Geophysical Prospecting

EAGE EUROPEAN ASSOCIATION OF GEOSCIENTISTS & ENGINEERS

Geophysical Prospecting, 2012, **60**, 201–216 doi: 10.1111/j.1365-2478.2011.00989.x

Estimation of geological dip and curvature from time-migrated zero-offset reflections in heterogeneous anisotropic media

Martin Tygel[1*], Bjørn Ursin[2], Einar Iversen[3] and Maarten V. de Hoop[4]

[1]*State University of Campinas (UNICAMP), Applied Mathematics Department, IMECC, 13083-859, Campinas SP, Brazil* [2]*Norwegian University of Science and Technology (NTNU), Department of Petroleum Engineering and Applied Geophysics, S.P. Andersensvei 15A, NO-7491 Trondheim, Norway* [3]*NORSAR, P.O. Box 53, 2027 Kjeller, Norway, and* [4]*Center for Computational and Applied Mathematics, Purdue University, 150 N. University Street, West Lafayete IN 47907, USA*

Received December 2009, revision accepted May 2011

ABSTRACT

Starting from a given time-migrated zero-offset data volume and time-migration velocity, recent literature has shown that it is possible to simultaneously trace image rays in depth and reconstruct the depth-velocity model along them. This, in turn, allows image-ray migration, namely to map time-migrated reflections into depth by tracing the image ray until half of the reflection time is consumed. As known since the 1980s, image-ray migration can be made more complete if, besides reflection time, also estimates of its first and second derivatives with respect to the time-migration datum coordinates are available. Such information provides, in addition to the location and dip of the reflectors in depth, also an estimation of their curvature. The expressions explicitly relate geological dip and curvature to first and second derivatives of reflection time with respect to time-migration datum coordinates. Such quantitative relationships can provide useful constraints for improved construction of reflectors at depth in the presence of uncertainty. Furthermore, the results of image-ray migration can be used to verify and improve time-migration algorithms and can therefore be considered complementary to those of normal-ray migration. So far, image-ray migration algorithms have been restricted to layered models with isotropic smooth velocities within the layers. Using the methodology of surface-to-surface paraxial matrices, we obtain a natural extension to smooth or layered anisotropic media.

Key words: Anisotropic media, Image ray migration, Image rays, Reflector dip and curvature, Time migration.

INTRODUCTION

Time migration, either post-stack or pre-stack, is widespread used in seismic processing to produce initial time-domain images and velocity in a simple and efficient way (Hubral and Krey 1980; Yilmaz 2000). Together with its advantages of computational efficiency and robustness with respect to a background velocity model, time migration has the drawback of producing distorted images, in some cases, even under mild lateral velocity variations (Robein 2003). An option to correct lateral positioning errors of time migration is to convert the time-migrated images into depth, which includes, as an obligatory step, the conversion of the time-migration velocities into a corresponding depth-velocity field.

We consider a seismic experiment where source and receiver locations have been mapped to a flat recording datum surface. On the other hand, time migration uses a flat time-migration datum surface on which the traces of the migrated data are specified. The two lateral coordinates along the recording datum surface and the recording time form the three-dimensional recording domain at zero source-receiver offset. A

* E-mail: mtygel@gmail.com

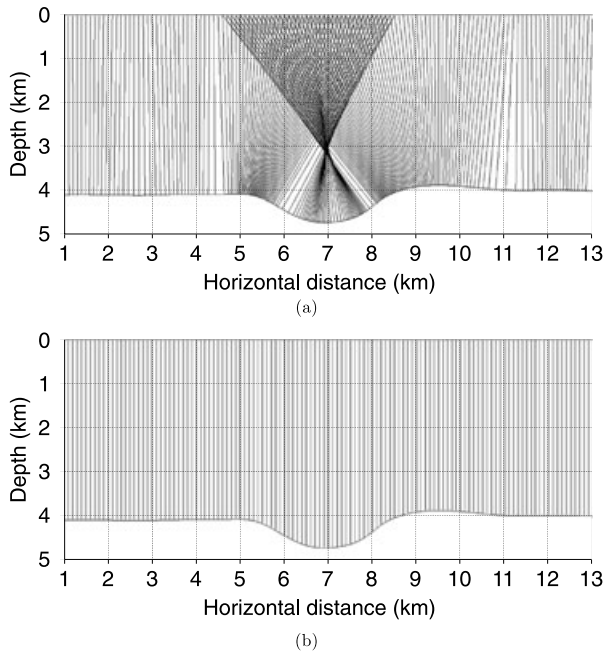

Figure 1 a) Normal-ray and b) image-ray trajectories for a syncline-shaped reflector in a homogeneous isotropic velocity field. The velocity is 2.5 km/s.

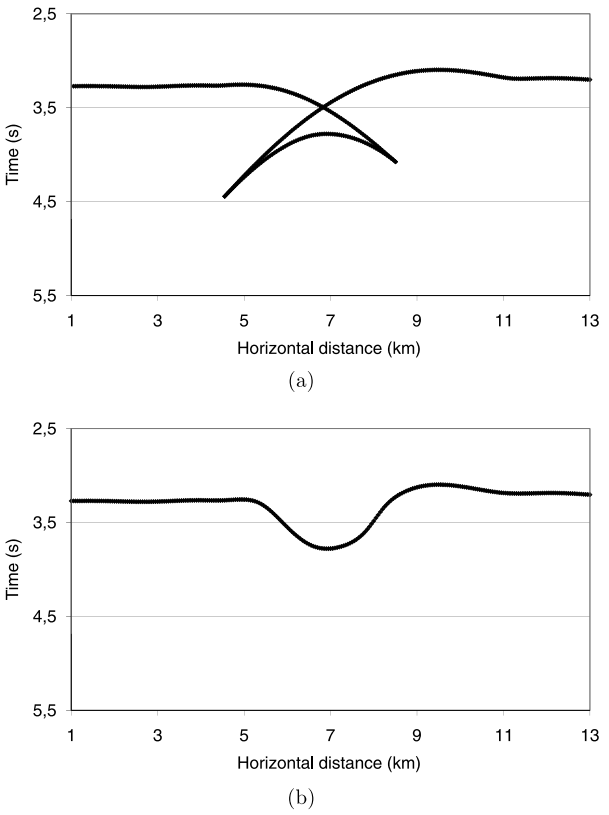

Figure 2 Two-way times, in a) the recording domain and b) the time-migration domain, corresponding to the ray fields shown in Fig. 1.

corresponding time-migration domain (at zero offset) is formed by the two coordinates in the time-migration datum surface and the migration time. For simplicity the two datum surfaces are assumed to coincide,— thus we refer to just datum surface in the following.

The theoretical explanation of the time-migration procedure has been given in Hubral (1977) by means of the concept of image rays. For an isotropic medium, the image ray starts normally to the datum surface and travels down to hit, generally non-normally, the (selected) reflector. In this way, it can be seen as complementary to a normal ray, which starts, generally non-normally, at the datum surface and hits normally the reflector. For an anisotropic medium, the notion of normal pertain to the phase directions.

A better insight on the advantages and limitations on the time-migration process can be gained by simple numerical simulations. In Fig. 1 we show normal- and image-ray fields for a syncline-shape reflector situated in a homogeneous and isotropic depth-velocity field. The normal-ray trajectories in Fig. 1(a) are normal to the reflector, whereas the image-ray trajectories in Fig. 1(b) are perpendicular to the datum surface. Corresponding reflection times computed by ray tracing are shown in Fig. 2. We note a triplication in the recording domain (Fig. 2a) and a single-valued reflector image in the time-migration domain (Fig. 2b). The introduction of a caustic in the image-ray field implies that there is no longer a one-to-one correspondence between points in the depth domain and the time-migration domain. Caustics and triplications in the image-ray field are therefore incompatible with the basic assumptions inherent to seismic time migration. As a consequence, it is mandatory to smooth the depth-velocity field to ensure that the mentioned one-to-one correspondence between the domains is not violated.

Recently, Cameron *et al.* (2006, 2007) unveiled the theoretical relationship between time-migration and time-interval velocities and presented algorithms to trace image rays from a given time-migration velocity field. A modified algorithm for the same purposes has been also presented in Iversen and Tygel (2008). Application of the theory to actual time-to-depth conversion has been presented in Cameron *et al.* (2008). The above papers show that isotropic depth velocities and also image rays can be constructed from a given time-migration velocity field. As a consequence, individual time-migrated reflections can be readily converted into depth by simply moving time samples along the image ray.

As well recognized in the seismic literature, more detailed velocity information and images can be gained if not only traveltimes but also slopes and curvatures (e.g., first and second derivatives of traveltime with respect to recording coordinates) are estimated from the data. Examples in this direction include, among others, plane-wave destructors (Claerbout 1992; Fomel 2002), time-domain seismic imaging using local event slopes (Douma and de Hoop 2006; Fomel 2007), the common-reflection-surface (CRS) stacking method (Hertweck *et al.* 2004) and the multifocus (MF) stacking method (Landa *et al.* 1999), as well as macro-velocity model building by the methods of stereotomography (Bilette and Lambaré 1998) and Normal-Incidence-Point (NIP)-wave tomography (Iversen and Gjøystdal 1984; Duveneck 2004). On the modeling side, we mention that reflector curvatures can be used in the study of deformation of geological surfaces and analyzing the folding or faulting of the interface between adjacent layers (see, e.g., Samson and Mallet 1997).

Under a given depth-velocity model, the problem of deriving the position, dip and curvature of a reflector in depth from measurements of reflection time and its first and second derivatives has a long history in the literature. For the case of normal-incidence non-converted primary reflections in isotropic media, a solution has been given in Kleyn (1977) (see also references therein). Ursin (1982) extended that solution to finite-offset reflections and incorporated estimation of reflector curvatures. The procedure to convert a reflection traveltime to the reflector in depth along normal-incidence rays is referred to as normal-ray migration or, simply, as map migration.

In general, map migration and forward modeling are combined for the purpose of inverting a depth-velocity model from a set of observed reflections. Iterative use of forward modelling and map migration, together with an error optimization scheme are combined to update a given depth-velocity model until the forward modeling of the reflectors honor the observed reflection data. A typical situation is the inversion of depth models with some a priori structure, e.g., homogeneous isotropic layers with curved interfaces, see Hubral and Krey (1980), Gjøystdal and Ursin (1981). Extensions allowing velocity gradients in the layers are given in Iversen and Gjøystdal (1984) and Biloti *et al.* (2002). A discussion of such algorithms is outside the scope of this work. Although very attractive from the theoretical point of view, map migration from normal-incidence or common-shot reflections face challenges in their application because of their high dependency on a complete velocity model and the difficulties (e.g., multipathing and triplications) in identifying (picking) reflections and their first and second derivatives in the data.

Based on the more robust properties of time-migrated reflections (e.g., collapse of diffractions, untangle of triplications, and less sensitivity of a macro-velocity model), a similar algorithm, referred to as image-ray migration has been proposed by Hubral and Krey (1980). That process connects the time-migrated non-converted primary reflections to the reflector following downgoing image rays from the datum surface into depth. In this way, image-ray migration is very similar to normal-incidence migration, in which downgoing normal rays are used to reach the reflector. Also for a depth model of homogeneous isotropic layers with curved interfaces, Hubral and Krey (1980)'s algorithm was able to depth propagate non-converted primary reflections in the time-migration domain. In later studies (Iversen *et al.* 1987, 1988) image-ray migration is extended to models with heterogeneous isotropic layers.

Image-ray migration is founded on consistency with respect to the time-migration process previously applied to the seismic data. Errors and inconsistencies introduced by time-migration will therefore propagate into the results of the subsequent image-ray migration. On the other hand, this can be turned into something positive: one can foresee that the results of image-ray migration are used to verify and improve time-migration algorithms. In that perspective, the image-ray mapping results will be complementary to those obtained by normal-ray migration.

We use in the derivation the powerful techniques of surface-to-surface paraxial matrices (see, e.g., Bortfeld 1989; Červený 2001; Moser and Červený 2007) to suitably modify and extend the image ray migration algorithm to account for full anisotropy and heterogeneity. We remark that the adopted term 'surface-to-surface paraxial matrix' used in this work has been introduced by Moser and Červený (2007) to replace the older and more commonly used term 'surface-to-surface propagator matrix'. Technical reasons for doing so can be found in that publication. The proposed methodology is illustrated using synthetic data sets for a single-interface 2D anisotropic model and a multi-layered 3D isotropic model. Results obtained by these first and basic applications are very encouraging.

PARAMETERS OF ZERO-OFFSET REFLECTIONS IN THE TIME-MIGRATION DOMAIN

Routinely applied to recorded seismic data, stacking to zero offset (e.g., by the common-midpoint (CMP) method) and

subsequent poststack time migration are able to produce first time images of the subsurface in a robust and efficient way. Stacking transforms the recorded data, defined in terms of trace location (i.e., source-receiver midpoint and half-offset) and time, into a simulated recording-domain volume at zero offset in terms of trace location (CMP coordinates) and recording time. In the same way, pre-stack time migration and subsequent stacking transforms the recorded data into a zero-offset time-migration domain (also a volume), defined by trace location (e.g., common-image-gather (CIG) coordinates) and migration time. More specifically, at least for primary events, zero-offset stacking (respectively, prestack time migration + zero-offset stacking) transforms recorded reflections at finite offsets into corresponding reflections under normal-incidence (respectively, image-ray) illumination. In a sense, both procedures can be seen as data reduction transformations from the five-dimensional recording domain into the three-dimensional recording or time-migration domains at zero offset.

From now on, we will restrict our attention to non-converted zero-offset reflections in the time-migration domain. In this context, the (two-way) traveltime for a fixed reflector, $T^M(\mathbf{m})$, will be described by the second-order Taylor expansion

$$T^M(\mathbf{m}) = T_0^M + \mathbf{m}^T\mathbf{p}^M + \frac{1}{2}\mathbf{m}^T\mathbf{M}^M\mathbf{m}. \qquad (1)$$

in which $\mathbf{m} = (m_1, m_2)^T$ specifies the trace location along the datum surface, $\mathcal{M}$. The approximation is valid in the vicinity of a reference trace, for simplicity taken at the origin $\mathbf{m} = \mathbf{0}$. Moreover the coefficients

$$T_0^M, \quad \mathbf{p}^M = \left(\frac{\partial T^M}{\partial m_I}\right), \quad \text{and} \quad \mathbf{M}^M = \left(\frac{\partial^2 T^M}{\partial m_I \partial m_J}\right), \qquad (2)$$

are reflection-time parameters evaluated at $\mathbf{m} = \mathbf{0}$. $T^M(\mathbf{m})$ can be interpreted as twice the traveltime along the image ray from the initial point with coordinate $\mathbf{m}$ on the datum surface to the point where it hits the reflector, the image-ray incidence point (IIP). Also, $T_0^M = T^M(\mathbf{0})$ represents the same quantity computed at the reference point.

Throughout this paper, the traveltime, T_0^M, as well as the linear (slope) and quadratic (curvature) parameters, $\mathbf{p}^M$ and $\mathbf{M}^M$, in equation (2) are considered as measured quantities. It is our aim to characterize the geometric attributes, namely dip and curvature of the reflector at the IIP in depth, as functions of the reflection-time parameters T_0^M, $\mathbf{p}^M$ and $\mathbf{M}^M$.

COORDINATE SYSTEMS

The formulation of our problem requires an adequate selection of coordinates. Here, we will consider, besides coordinates at the datum and reflector surfaces, also auxiliary so-called wavefront coordinates.

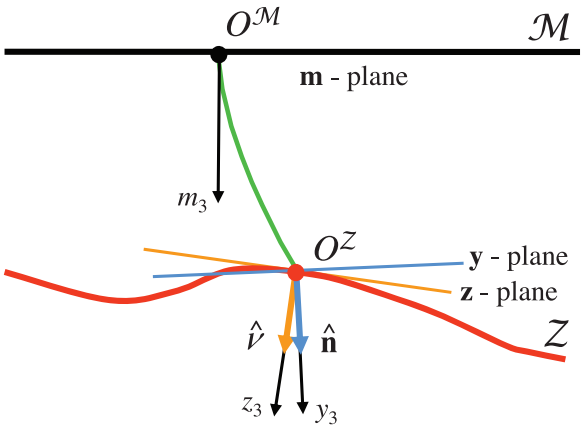

Figure 3 Image ray (green) between the point $O^{\mathcal{M}}$ in the datum surface $\mathcal{M}$ (black) and the point $O^{\mathcal{Z}}$ in the reflector surface $\mathcal{Z}$ (red). Associated quantities defined in the text: local Cartesian coordinates at datum (**m** and m_3), reflector (**z** and z_3), and wavefront (**y** and y_3); unit normals to wavefront ($\hat{\mathbf{n}}$) and reflector ($\hat{\boldsymbol{\nu}}$).

Datum and reflector coordinates

Referring to Fig. 3, points on the datum surface, $\mathcal{M}$, and the reflector, $\mathcal{Z}$, in the vicinity of the initial and final points of a selected reference (central) image ray will be specified by local 3D Cartesian systems, $\hat{\mathbf{m}} = (m_1, m_2, m_3)^T$ and $\hat{\mathbf{z}} = (z_1, z_2, z_3)^T$, respectively. Correspondingly, we also use the simplifying notations $\mathbf{m} = (m_1, m_2)^T$ and $\mathbf{z} = (z_1, z_2)^T$. These systems will be referred to as *datum* and *reflector* coordinate systems. For time-migration, it is common to take the datum surface as planar horizontal, to avoid surface-induced image distortions. Figure 3 depicts this usual scenario, adopted in this work.

The $\hat{\mathbf{m}}$-system has its origin at the initial point, $O^{\mathcal{M}}$, of the reference image ray on the datum surface. The m_3-axis points in the direction of the surface normal to $\mathcal{M}$ at $O^{\mathcal{M}}$, namely, vertically down. Moreover, the (orthogonal) m_1- and m_2-axes lie at $\mathcal{M}$, so as to form a right-handed Cartesian (m_1, m_2, m_3) system. We note that the orientations of the axes m_1 and m_2 are unique only up to a rotation around the m_3-axis.

The $\hat{\mathbf{z}}$-system has its origin at the endpoint, $O^{\mathcal{Z}} = \text{IIP}$, of the central image ray and its axis z_3 points in the direction of the normal of $\mathcal{Z}$ at $O^{\mathcal{Z}}$. The remaining (z_1- and z_2-) axes lie on the tangent plane to $\mathcal{Z}$ at $O^{\mathcal{Z}}$. The locations of the axes z_1 and z_2 are unique up to an arbitrary rotation about the reflector normal (z_3-axis). In local Cartesian reflector coordinates, the

reflector is assumed in the form

$$z_3 = \Sigma^{\mathcal{Z}}(\mathbf{z}), \tag{3}$$

with the properties

$$\Sigma^{\mathcal{Z}}(\mathbf{0}) = 0, \quad \frac{\partial \Sigma^{\mathcal{Z}}}{\partial \mathbf{z}}(\mathbf{0}) = \mathbf{0}, \quad \text{and} \quad \frac{\partial^2 \Sigma^{\mathcal{Z}}}{\partial \mathbf{z} \partial \mathbf{z}^T}(\mathbf{0}) = -\mathbf{D}, \tag{4}$$

where $\mathbf{D}$ is the reflector curvature matrix. The two left-most equations above incorporate the fact that the reflector is tangent to the plane formed by the z-coordinates at the origin, $O^{\mathcal{Z}}$.

We observe that, although the system $\hat{\mathbf{m}}$ can be readily constructed on the (known) datum surface, this is not the case for the $\hat{\mathbf{z}}$-system, constructed on the (unknown) reflector. As seen below, the $\hat{\mathbf{z}}$ system (together with the reflector dip at $O^{\mathcal{Z}}$) will be determined from the knowledge of T_0^M, $\mathbf{p}^M$. The reflector curvature at $O^{\mathcal{Z}}$ will additionally require the matrix $\mathbf{M}^M$.

Wavefront coordinate system

As indicated above, we assume that a depth-velocity model is known. The image-ray incidence point, $O^{\mathcal{Z}}$, can also be considered known. It is obtained by following the central image ray trajectory until the time $t = T_0^M/2$ is consumed. Moreover, the slowness vector, $\hat{\mathbf{p}}$, is normal to the wavefront at $O^{\mathcal{Z}}$ so that

$$\hat{\mathbf{p}} = \frac{1}{c}\hat{\mathbf{n}}, \tag{5}$$

where $\hat{\mathbf{n}}$ denotes the wavefront unit normal and c is the phase velocity.

We introduce a local Cartesian wavefront coordinate system, $\hat{\mathbf{y}} = (y_1, y_2, y_3)^T$, with origin at the point $O^{\mathcal{Z}}$ (Fig. 3), defined such that the y_3 axis is parallel to the wavefront unit normal vector, $\hat{\mathbf{n}}$. Quantities belonging to the wavefront coordinate system are denoted with a superscript Y. In particular, for the slowness and ray-velocity (group-velocity) vectors $\hat{\mathbf{p}}^Y$ and $\hat{\mathbf{v}}^Y$ we have

$$\hat{\mathbf{p}}^Y = \begin{pmatrix} \mathbf{0} \\ 1/c \end{pmatrix}, \qquad \hat{\mathbf{v}}^Y = \begin{pmatrix} \mathbf{v}^Y \\ c \end{pmatrix}. \tag{6}$$

The vector $\mathbf{v}^Y$ is zero if the medium is isotropic at $O^{\mathcal{Z}}$.

RELATIONS BETWEEN WAVEFRONT AND REFLECTOR COORDINATES

Following Červený (2001) the transformation from local wavefront to reflector coordinates is described to the first order by the relation

$$\hat{\mathbf{z}} = \hat{\mathbf{G}}\hat{\mathbf{y}}. \tag{7}$$

Being a coordinate transformation between Cartesian coordinate systems, matrix $\hat{\mathbf{G}}$ is an orthonormal rotation matrix. As such, it satisfies the relation $\hat{\mathbf{G}}^{-1} = \hat{\mathbf{G}}^T$, and also

$$\hat{\mathbf{G}}\hat{\mathbf{G}}^T = \hat{\mathbf{G}}^T\hat{\mathbf{G}} = \hat{\mathbf{I}}, \tag{8}$$

in which $\hat{\mathbf{I}}$ is the 3×3 identity matrix. The matrix $\hat{\mathbf{G}}$ has as columns the unit vectors of the wavefront coordinate system expressed with respect to the reflector coordinate system. The third column of matrix $\hat{\mathbf{G}}$ is therefore a unit vector normal to the wavefront in $\hat{\mathbf{z}}$-coordinates. That vector is denoted by $\hat{\mathbf{n}}^Z = (n_1^Z, n_2^Z, n_3^Z)^T$, where the superscript Z signifies that the vector belongs to the reflector coordinate system. The same vector, not referred to a coordinate system, is denoted by $\hat{\mathbf{n}}$. In the same way, the orthonormality of matrix $\hat{\mathbf{G}}$ (equation (8)), implies that the third row of that matrix is given by the transpose of the unit vector normal to the reflector, expressed in $\hat{\mathbf{y}}$-coordinates, namely $\hat{\boldsymbol{\nu}}^Y = (\nu_1^Y, \nu_2^Y, \nu_3^Y)^T$. The same vector, not referred to a coordinate system, is denoted by $\hat{\boldsymbol{\nu}}$. The first two-component versions of the above vectors are denoted by $\mathbf{n}^Z$, $\boldsymbol{\nu}^Y$, $\mathbf{n}$, $\boldsymbol{\nu}$, respectively. Vector $\hat{\boldsymbol{\nu}}$ is very important as it defines the reflector dip. Note especially that

$$\nu_3^Y = n_3^Z = \hat{\mathbf{n}}^T\,\hat{\boldsymbol{\nu}} \neq 0. \tag{9}$$

The last inequality above follows from the assumption that the central image ray hits the reflector. As such, the vectors $\hat{\mathbf{n}}$ and $\hat{\boldsymbol{\nu}}$ cannot be perpendicular. In accordance with Červený (2001), we let $\mathbf{G}$ denote the 2×2 upper left sub-matrix of matrix $\hat{\mathbf{G}}$. Moreover, we adopt the form of matrix $\hat{\mathbf{G}}$ used by Iversen (2005),

$$\hat{\mathbf{G}} = \begin{pmatrix} \mathbf{G} & \mathbf{n}^Z \\ \boldsymbol{\nu}^{YT} & G_{33} \end{pmatrix}, \tag{10}$$

where the two-component vector, $\boldsymbol{\nu}^Y$, is the projection of the full reflector normal, $\hat{\boldsymbol{\nu}}^Y$, onto the $\mathbf{y}$-plane, and $G_{33} = n_3^Z = \nu_3^Y$. Setting

$$\mathbf{f} = -\frac{\boldsymbol{\nu}^Y}{\nu_3^Y}, \quad \text{with} \quad \nu_3^Y = \pm\frac{1}{\sqrt{1 + \mathbf{f}^T\mathbf{f}}}, \tag{11}$$

the reflector normal can be given as

$$\hat{\boldsymbol{\nu}}^Y = \nu_3^Y \begin{pmatrix} -\mathbf{f} \\ 1 \end{pmatrix}. \tag{12}$$

Note that a convention for the vector direction must be specified. By selecting '+' or '−' the reflector normal will be pointing in the same or opposite direction to that of the image-ray

slowness vector, that means, down and up, respectively. By substituting expression 10 into the far-left equation (8), one has, after some small rearrangement, the relationship

$$\mathbf{p}^Z = \frac{1}{c}\mathbf{G}\mathbf{f}. \tag{13}$$

Determination of matrix $\hat{\mathbf{G}}$

We briefly discuss how to determine the matrix $\hat{\mathbf{G}}$ and start by recalling that the vector $\hat{\boldsymbol{\nu}}^Y$ coincides with the z_3-axis of the $\hat{\mathbf{z}}$-system. The specification of the two remaining (z_1, z_2)-axes can be constructed according to any preferred convention, as long as to make up a right-handed Cartesian system. Note especially that it is not necessary to require the local reflector coordinate system to be aligned with the plane of incidence. A simple choice for the coordinate axis $(\hat{\mathbf{z}}_1, \hat{\mathbf{z}}_2, \hat{\mathbf{z}}_3)$ of the $\hat{\mathbf{z}}$-system is to set $\hat{\mathbf{z}}_3 = \hat{\boldsymbol{\nu}}$ and to define the remaining axes as

$$\hat{\mathbf{z}}_1 = \frac{\hat{\mathbf{y}}_2 \times \hat{\boldsymbol{\nu}}}{|\hat{\mathbf{y}}_2 \times \hat{\boldsymbol{\nu}}|} \quad \text{and} \quad \hat{\mathbf{z}}_2 = \hat{\boldsymbol{\nu}} \times \hat{\mathbf{z}}_1. \tag{14}$$

The above definitions yield

$$\begin{aligned}\hat{\mathbf{G}} &= \left(\hat{\mathbf{z}}_1^Y \quad \hat{\mathbf{z}}_2^Y \quad \hat{\mathbf{z}}_3^Y\right)^T \\ &= \begin{pmatrix} \dfrac{\nu_3^Y}{a} & 0 & -\dfrac{\nu_1^Y}{a} \\ -\dfrac{\nu_1^Y \nu_2^Y}{a} & a & -\dfrac{\nu_2^Y \nu_3^Y}{a} \\ \nu_1^Y & \nu_2^Y & \nu_3^Y \end{pmatrix}, \quad \text{with} \quad a = \sqrt{\nu_1^{Y2} + \nu_3^{Y2}}.\end{aligned} \tag{15}$$

Note, in particular, that if $\hat{\mathbf{n}}$ is parallel to $\hat{\mathbf{z}}_3$, the transformation matrix reduces to the identity matrix, $\hat{\mathbf{G}} = \hat{\mathbf{I}}$.

SURFACE-TO-SURFACE PARAXIAL MATRIX

For various purposes, it is convenient to introduce the 4 × 4 surface-to-surface paraxial matrix of the one-way central (downgoing) image ray

$$\mathbf{T} = \begin{pmatrix} \boldsymbol{\mathcal{A}} & \boldsymbol{\mathcal{B}} \\ \boldsymbol{\mathcal{C}} & \boldsymbol{\mathcal{D}} \end{pmatrix}, \tag{16}$$

in which $\boldsymbol{\mathcal{A}}$, $\boldsymbol{\mathcal{B}}$, $\boldsymbol{\mathcal{C}}$ and $\mathbf{D}$ are 2 × 2 matrix components. The surface-to-surface paraxial matrix, $\mathbf{T}$ establishes a linear relationship

$$\begin{pmatrix} \delta\mathbf{z} \\ \delta\mathbf{p}^Z \end{pmatrix} = \mathbf{T} \begin{pmatrix} \delta\mathbf{m} \\ \delta\mathbf{p}^M \end{pmatrix}, \tag{17}$$

between the 4 × 1 dislocation vectors in position and slowness of the paraxial and reference image rays, $\delta(m_1, m_2, p_1^M, p_2^M)^T$ and $\delta(z_1, z_2, p_1^Z, p_2^Z)^T$, respectively at their initial points on the (known) datum surface, $\mathcal{M}$, and endpoints on the (unknown) reflector, $\mathcal{Z}$. Detailed descriptions and applications of the surface-to-surface paraxial matrix concept can be found in e.g., Bortfeld (1989), Schleicher *et al.* (2007) and Moser and Červený (2007).

Following (Červený 2001), the wavefront coordinate system allows for the computation of the submatrix systems $(\mathbf{Q}_1, \mathbf{P}_1)$ and $(\mathbf{Q}_2, \mathbf{P}_2)$, which correspond to hypothetical wavefront solutions initialized in the same point as an 'exploding' plane (subscript 1) and a point explosion (subscript 2). The two solutions form the 4 × 4 ray-propagator matrix,

$$\boldsymbol{\Pi} = \begin{pmatrix} \mathbf{Q}_1 & \mathbf{Q}_2 \\ \mathbf{P}_1 & \mathbf{P}_2 \end{pmatrix}, \tag{18}$$

defined with respect to initial and final wavefront tangent planes at the points $O^{\mathcal{M}}$ and $O^{\mathcal{Z}}$ on the central image ray. As such, the matrix $\boldsymbol{\Pi}$ is an inherent property of this image ray, defined independently of the reflector.

The introduction of the $\hat{\mathbf{y}}$-system enables the decomposition of the paraxial matrix in the form

$$\mathbf{T} = \mathbf{Y}\boldsymbol{\Pi}, \tag{19}$$

where $\mathbf{Y}$ is the so-called projection matrix, which embodies the properties of the reflector and provides the link between the paraxial matrices $\mathbf{T}$ and $\boldsymbol{\Pi}$. With the help of the matrix $\hat{\mathbf{G}}$, we can obtain an explicit expression of the projection matrix, $\mathbf{Y}$, included in equation (19). It is given by (Červený 2001, equation 4.14.68)

$$\mathbf{Y} = \begin{pmatrix} (\mathbf{G} - \mathbf{A}^{an})^{-T} & 0 \\ (\mathbf{E} - p_3^Z \mathbf{D})\,(\mathbf{G} - \mathbf{A}^{an})^{-T} & (\mathbf{G} - \mathbf{A}^{an}) \end{pmatrix}, \tag{20}$$

where the superscript $-T$ denotes the transpose of the inverse. The 2 × 2 matrix $\mathbf{E}$, referred to as the *inhomogeneity matrix* (Červený 2001, equation 4.14.55), is given by

$$\begin{aligned} E_{IJ} = \frac{1}{c}\Big[& G_{I3} G_{JM}\, \eta_M^Y + G_{J3} G_{IK}\, \eta_K^Y \\ & + G_{I3} G_{J3} \left(\eta_3^Y - \frac{1}{c}\eta_L^Y v_L{}^Y\right)\Big], \end{aligned} \tag{21}$$

in which $I, J, K, L, M = 1, 2$ and Einstein's summation convention is assumed. The symbol $\mathbf{A}^{an}$ stands for the 2 × 2 anisotropy matrix (Červený 2001, equation 4.14.56),

$$\mathbf{A}^{an} \equiv \mathbf{p}^Z \mathbf{v}^{Y\,T} = \frac{1}{c}\mathbf{G}\mathbf{f}\mathbf{v}^{Y\,T}, \tag{22}$$

where equation (13) has been also used. The entities $v_i{}^Y$ and $\eta_i{}^Y$, $i = 1, 2, 3$, are components of the ray-velocity vector $\hat{\mathbf{v}}^Y$

and the 'eta vector' $\hat{\boldsymbol{\eta}}^Y = d\hat{\mathbf{p}}^Y/dt$ (derivative of slowness vector with respect to traveltime) specified in wavefront coordinates (Červený 2001, equation 4.14.12). For isotropic media, we have $\mathbf{A}^{an} = \mathbf{0}$. It is to be observed that in many situations, one can also consider that $\mathbf{E} = \mathbf{0}$. For example, this is the case if the medium is locally homogeneous. The matrix $\mathbf{E}$ is also zero if the slowness vector is normal to the reflector.

Inserting the projection matrix equation (20) into the decomposition equation (19), the paraxial matrix components can be recast as

$$\boldsymbol{\mathcal{A}} = (\mathbf{G} - \mathbf{A}^{an})^{-T}\mathbf{Q}_1, \tag{23}$$

$$\boldsymbol{\mathcal{C}} = \left(\mathbf{E} - p_3^Z\mathbf{D}\right)\boldsymbol{\mathcal{A}} + \boldsymbol{\mathcal{A}}^{-T}\mathbf{Q}_1{}^T\mathbf{P}_1, \tag{24}$$

and similarly

$$\boldsymbol{\mathcal{B}} = (\mathbf{G} - \mathbf{A}^{an})^{-T}\mathbf{Q}_2, \tag{25}$$

$$\boldsymbol{\mathcal{D}} = \left(\mathbf{E} - p_3^Z\mathbf{D}\right)\boldsymbol{\mathcal{B}} + \boldsymbol{\mathcal{B}}^{-T}\mathbf{Q}_2{}^T\mathbf{P}_2. \tag{26}$$

EXPRESSIONS FOR REFLECTOR DIP AND CURVATURE

The one-way traveltime along image rays from the datum surface to the reflector is denoted here as $\mathcal{T}(\mathbf{m})$. In Appendix A we derive fundamental equations for the first and second derivatives of the function $\mathcal{T}$. These relations are used in the following to obtain expressions for dip and curvature of the reflector. The key relationship in this context is the condition

$$T^M(\mathbf{m}) = 2\mathcal{T}(\mathbf{m}), \tag{27}$$

which we differentiate twice with respect to coordinates (m_1, m_2) and evaluate at $\mathbf{m} = 0$.

Reflector dip

The reflector dip $\mathbf{f}$, in wavefront coordinates, has to satisfy equation (13) derived above. Moreover, by applying the condition (27) to the fundamental relation (A14) involving the surface-to surface traveltime gradient we obtain

$$\mathbf{p}^Z = \frac{1}{2}\boldsymbol{\mathcal{A}}^{-T}\mathbf{p}^M, \tag{28}$$

where $\mathbf{p}^M = \partial T^M/\partial\mathbf{m}$ is assumed known. We shall also need equations (22) and (23) specifying, respectively, the matrices $\mathbf{A}^{an}$ and $\boldsymbol{\mathcal{A}}$. Combining all this yields the result

$$\mathbf{f} = \frac{c}{2}(1+\kappa)^{-1}\mathbf{Q}_1^{-T}\mathbf{p}^M, \tag{29}$$

where the scalar κ has the definition

$$\kappa = \frac{1}{2}\mathbf{v}^{Y\,T}\mathbf{Q}_1^{-T}\mathbf{p}^M. \tag{30}$$

If the medium is isotropic at the point O^Z, we have $\kappa = 0$.

Taken into account equations (11) and (12), the sought-for reflector unit normal, $\hat{\mathbf{v}}$, is obtained. The transformation matrix $\hat{\mathbf{G}}$ can also be computed, e.g., using equation (15). Knowing $\hat{\mathbf{G}}$ we can obtain matrices $\mathbf{E}$, $\mathbf{A}^{an}$, and $\boldsymbol{\mathcal{A}}$, which are needed for estimation of reflector curvature.

Reflector curvature

In the following we use equations (A23) and (A24) from Appendix A which connect the curvature matrix to second derivatives of surface-to-surface traveltime. Taking into account the condition (27), we obtain

$$\frac{1}{2}\mathbf{M}^M = \boldsymbol{\mathcal{A}}^T\left(\mathbf{E} + \boldsymbol{\mathcal{A}}^{-T}\mathbf{Q}_1^T\mathbf{P}_1\boldsymbol{\mathcal{A}}^{-1} - \frac{1}{v_3^Z}\mathbf{D}\right)\boldsymbol{\mathcal{A}}. \tag{31}$$

Minor rearranging of equation (31) then yields

$$\mathbf{D} = v_3^Z\left[\mathbf{E} + \boldsymbol{\mathcal{A}}^{-T}\left(\mathbf{Q}_1^T\mathbf{P}_1 - \frac{1}{2}\mathbf{M}^M\right)\boldsymbol{\mathcal{A}}^{-1}\right]. \tag{32}$$

It may be desirable to express the component v_3^Z in terms of the scalar κ defined in equation (30). This yields (see Appendix B)

$$v_3^Z = \frac{c\,n_3^Z}{1+\kappa}, \tag{33}$$

where n_3^Z is given by equation (9).

Equation (32) provides the sought-for reflector curvature, thus completing the solution of our problem. As a byproduct,

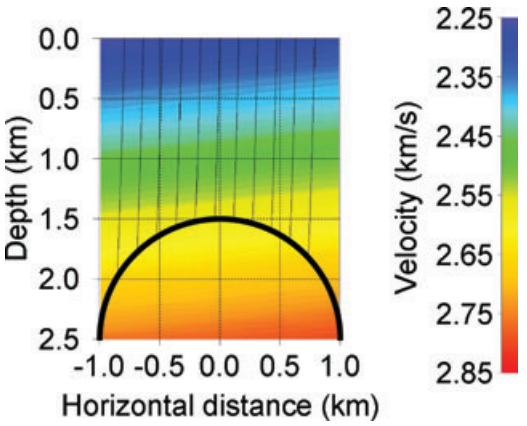

Figure 4 Experiment 1: Cylindrical reflector situated in a heterogeneous tilted transversely isotropic medium. Image ray trajectories used for generation of 'observed' two-way times in the time-migration domain are superimposed.

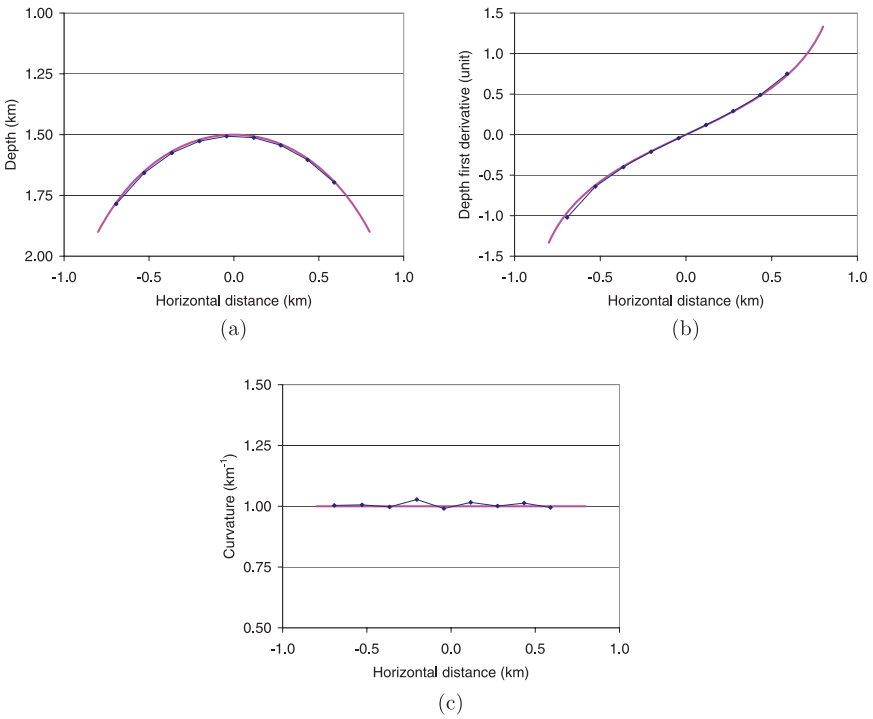

Figure 5 True (magenta) and estimated (blue) values of a) depths, b) dips and c) curvatures for the cylindrical reflector shown in Fig. 4. The true anisotropic velocity model was used for image-ray migration.

the knowledge of dip and curvature quantities allows us to obtain the complete surface-to-surface paraxial matrix of the central image ray, as specified above by equations (23)–(26).

Summarized procedure

It is instructive to summarize the obtained results in an algorithmic form. We assume that a depth-velocity model is available and an identified non-converted primary reflection within a zero-offset time-migrated data volume is given. For any given common-image gather location $O^{\mathcal{M}}$ in the datum surface we use known reflection-time parameters T_0^M, $\mathbf{p}^M$, and $\mathbf{M}^M$ (equation (2)) to compute the corresponding depth location, dip, and curvature at the image-ray incidence point, $O^{\mathcal{Z}}$.

i **Image-ray incidence point:** Starting at $O^{\mathcal{M}}$, trace the image ray downwards using the given depth-velocity model. Recall that the image ray has its phase direction normal to the datum surface at $O^{\mathcal{M}}$. The image ray reaches $O^{\mathcal{Z}}$ when half the given traveltime, $T_0^M/2$, is consumed. The ray-tracing procedure yields the slowness ($\hat{\mathbf{p}}$), ray-velocity ($\hat{\mathbf{v}}$), and eta ($\hat{\boldsymbol{\eta}}$) vectors at $O^{\mathcal{Z}}$;

ii **Wavefront coordinate system:** Construct the $\hat{\mathbf{y}}$-wavefront coordinate system, setting its origin at $O^{\mathcal{Z}}$ and the y_3-axis pointing in the direction of the slowness vector, $\hat{\mathbf{p}}$. Set the remaining axes, so as to make up a right-handed orthonormal system. Then compute the ray-velocity vector in $\hat{\mathbf{y}}$-coordinates, $\hat{\mathbf{v}}^Y$;

iii **Reflector dip vector:** The reflector dip vector, $\hat{\boldsymbol{\nu}}^Y$, is given by equation (12), once the vector $\mathbf{f}$ is obtained. That vector is computed using equations (29) and (30);

iv **Matrices $\mathbf{Q}_1$ and $\mathbf{P}_1$:** Still using the given depth-velocity model, apply dynamic ray tracing to determine the submatrix system ($\mathbf{Q}_1$, $\mathbf{P}_1$), which corresponds to the hypothetical wavefront solution initialized at the point $O^{\mathcal{M}}$ as an 'exploding' datum plane;

v **Matrices $\hat{\mathbf{G}}$ and $\boldsymbol{\mathcal{A}}$:** With the knowledge of the dip vector, matrix $\hat{\mathbf{G}}$ is computed by equation (15). Using matrix $\hat{\mathbf{G}}$ we compute the inhomogeneity matrix $\mathbf{E}$ (equation (21)) and the anisotropy matrix $\mathbf{A}^{an}$ (equation (22)) at $O^{\mathcal{Z}}$. Matrix $\boldsymbol{\mathcal{A}}$ is obtained by equation (23), with the help of equation (13);

vi **Reflector curvature matrix:** This matrix is computed by equation (32).

NUMERICAL EXAMPLES

In this section we present two numerical examples of mapping reflection-time parameters belonging to the time-migration domain to corresponding parameters in the depth domain,

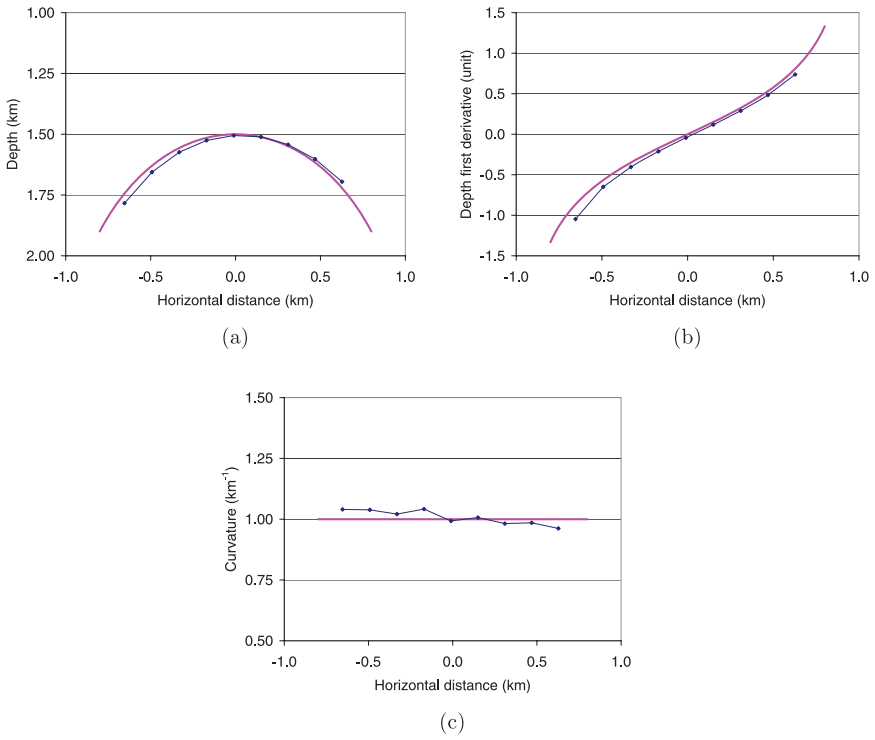

Figure 6 True (magenta) and estimated (blue) values of a) depths, b) dips and c) curvatures for the cylindrical reflector shown in Fig. 4. Anisotropy was ignored in the image-ray migration.

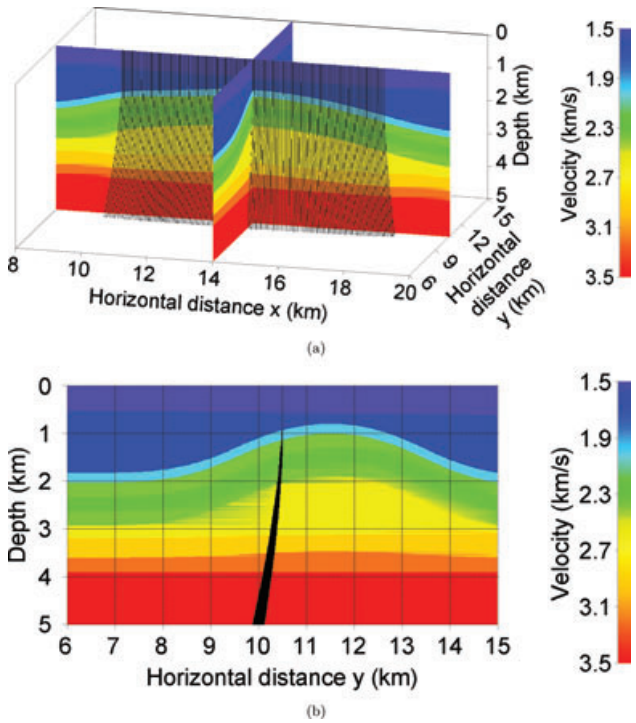

Figure 7 Experiment 2: a) 3D view of image ray trajectories starting along the line $y = 10.5$ (km) in the datum surface, b) projection of the same trajectories into the cross section $x = 14$ (km).

using a known macro-velocity depth model. Observe that depth-domain coordinates are from now on referred to as (x, y, z).

Experiment 1: 2D anisotropic model

Consider a cylindrical reflector situated in a smooth 2D anisotropic medium (Fig. 4). The anisotropy is of type TTI (tilted transversely isotropic) with a fixed symmetry axis in the direction specified by the vector $(u_x, u_y, u_z) = (0.1, 0, 1)$.

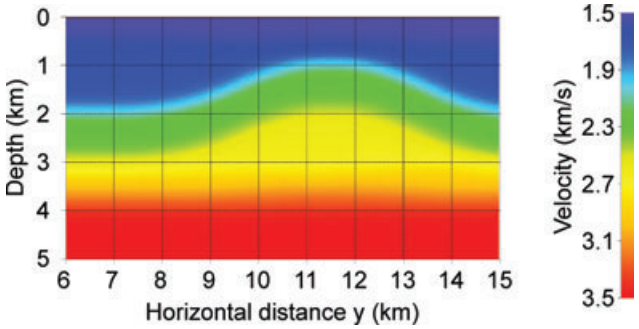

Figure 8 Cross section $x = 14$ (km) of the model in Fig. 7 after velocity smoothing with Hamming radius 0.8 km.

The P-wave velocity along this axis is given by the linear function $V_P(x, z) = 2.28 + 0.02x + 0.2z$ [km/s], while the corresponding S-wave velocities are computed using Poisson's ratio so that $V_S(x, z) = V_P(x, z)/\sqrt{3}$. Thomsen's parameters ϵ and δ have the values 0.2 and 0.1, respectively. The cylindrical reflector has its axis in the y-direction and a radius of 1 km. The axis passes through the reference point (0, 0, 2.5) (km).

To obtain synthetic measurements we traced image rays from the datum surface until they hit the cylinder. One can observe (Fig. 4) that the resulting ray trajectories are not perpendicular to the datum surface. Computed ray traveltimes were multiplied by two and used for generation of a cubic B-spline function. From this function we obtained 'measured'

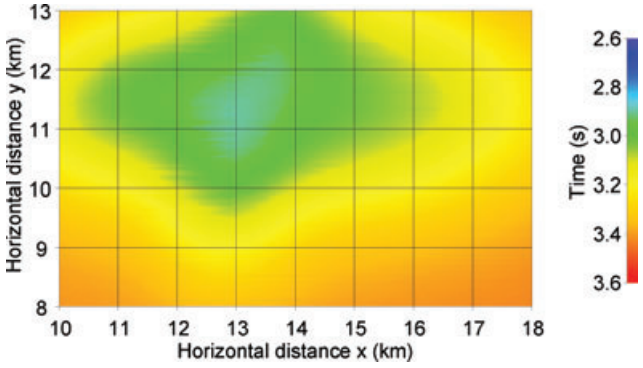

Figure 9 Simulated reflection time in the time-migration domain corresponding to the selected depth reflector, confined between the depths 2.97 and 3.27 km.

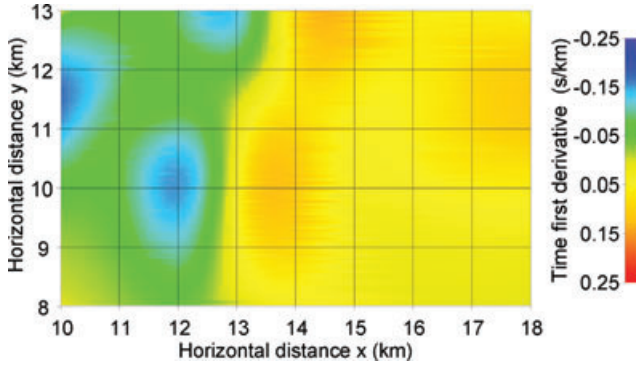

Figure 10 Slope x of the reflection time in Fig. 9.

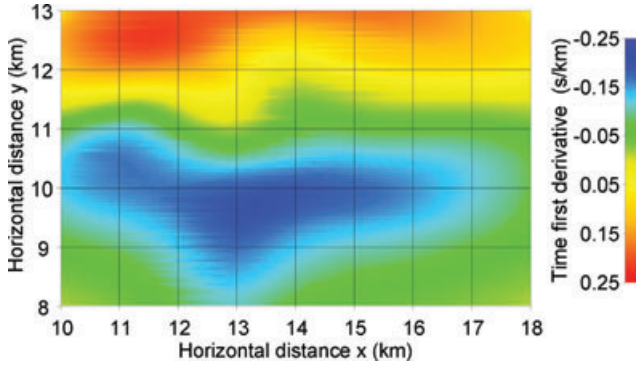

Figure 11 Slope y of the reflection time in Fig. 9.

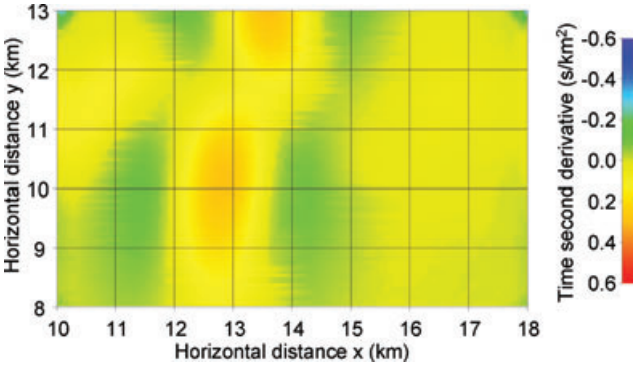

Figure 12 Second derivative xx of the reflection time in Fig. 9.

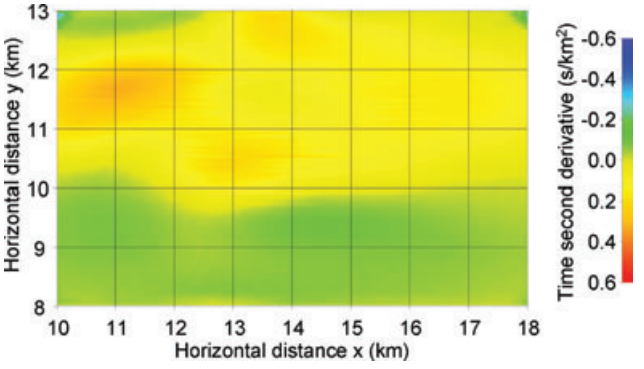

Figure 13 Second derivative yy of the reflection time in Fig. 9.

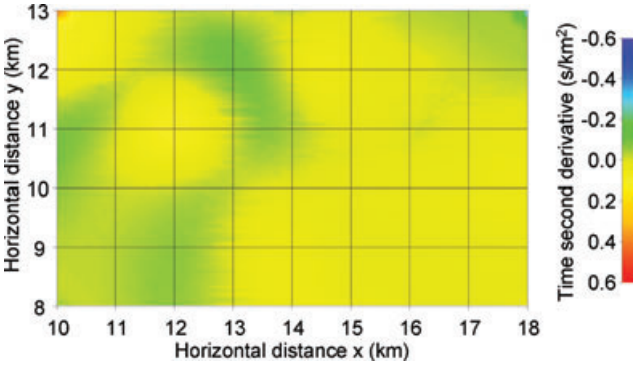

Figure 14 Second derivative xy of the reflection time in Fig. 9.

input parameters (times, slopes, and second derivatives) to be used for estimation of reflector depths, dips, and curvatures.

Figure 5 compares exact values of the cylinder depth, dip, and curvature to those estimated using our image-ray migration approach in the true velocity model. The theoretical results are confirmed through this example, but it is important to remark that the curvature estimation is particularly exposed to small numerical errors as well as to measurement errors. Therefore, to obtain reliable results in 'real' situations it will be critical to perform appropriate smoothing of the input time parameters. We also did an image-ray migration test where anisotropy was ignored in the velocity model (Fig. 6). One can then observe a significant mispositioning of the estimated reflector and corresponding systematic errors in estimated dip and curvature.

Experiment 2: 3D isotropic model

A 3D isotropic model (Fig. 7) containing planar and curved non-intersecting interfaces was chosen as the 'true' model. By tracing image rays in this layered model, we obtained reflection time maps in the time-migration domain, one such map for each model interface.

Although input reflection time maps were obtained using the layered model in Fig. 7, it is more natural for the image-ray migration procedure to use a velocity grid, as is common in time and depth migration. Appropriate smoothing of this depth-velocity field is a must. Here we used smoothing in the form of a repeated processing by a Hamming operator, applied independently to the various coordinate directions. This Hamming-operator smoothing is constrained by a certain aperture or radius, defined as the maximum distance within which a given data sample contributes to the smoothing of neighboring samples. For the model under consideration, the Hamming radius was set to 0.8 km. A cross section through the smoothed model is shown in Fig. 8, it is to be compared to the corresponding cross section through the layered model in Fig. 7(b).

Results of the image-ray migration procedure are presented here for one single reflector, namely, the one with

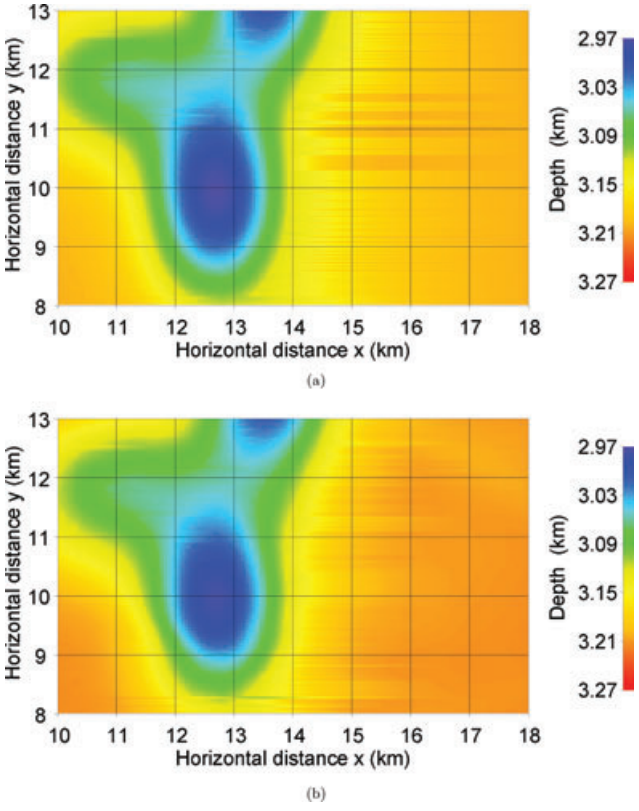

Figure 15 Depth a) of the true depth reflector and b) estimated by the image-ray migration method.

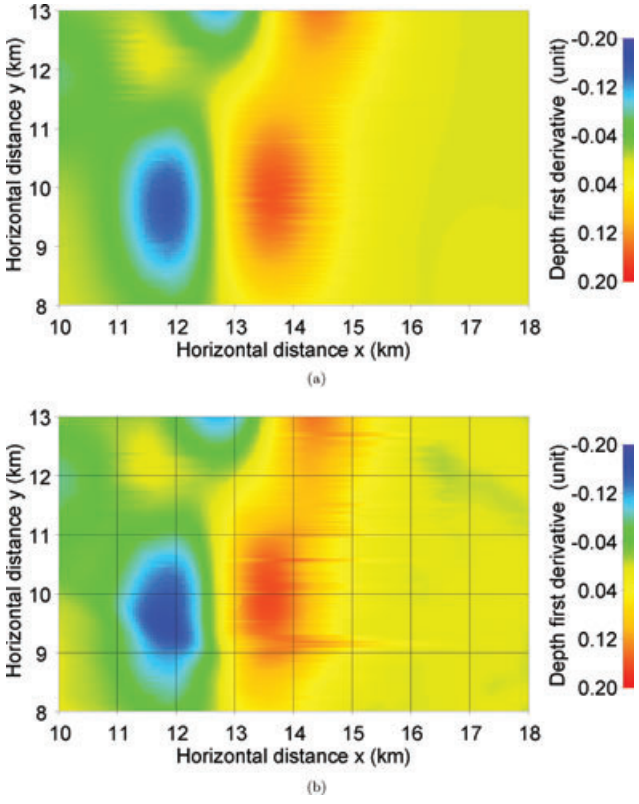

Figure 16 Dip *x* a) of the true depth reflector and b) estimated by the image-ray migration method.

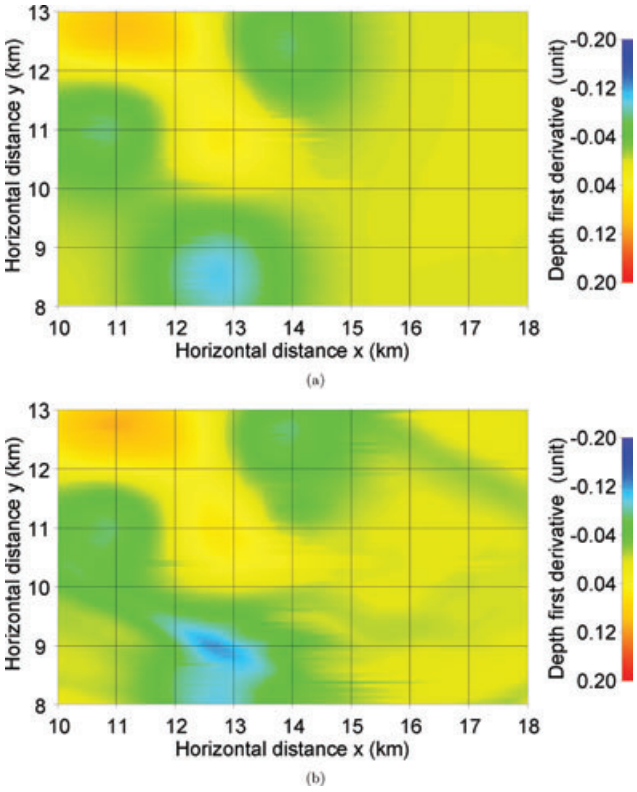

Figure 17 Dip *y* a) of the true depth reflector and b) estimated by the image-ray migration method.

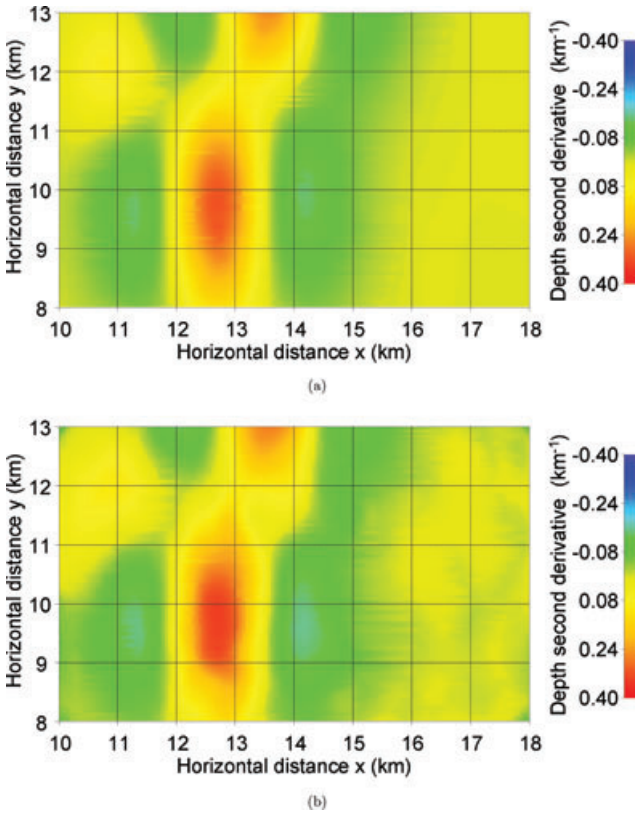

Figure 18 Second derivative *xx* a) of the true depth reflector and b) estimated by the image-ray migration method.

depths ranging between 2.97 and 3.27 km. The input reflection time parameters for this selected reflector are shown in Figs 9–14. The six input parameters are the reflection time, the slopes in the x and y directions, the main second derivatives (xx and yy), and finally the mixed second derivative (xy). In Figs 15–20 we compare parameters of the true depth reflector to those estimated by the image-ray migration. The parameters are the reflection depth, the reflector dips (x and y), and the associated second derivatives (xx, yy, xy).

The mean error in the estimated depth of the selected reflector is 9 m. This is to be compared to the mean depth of the reflector, which is 3152 m. Furthermore, comparison of the true and estimated first and second derivatives shows a high degree of consistency, thus indicating that the method has a good potential for success in practice, when applying a sufficiently smooth depth-velocity model. More smoothing is required to obtain consistent dips than consistent depths, and even more smoothing is required to obtain consistent second derivatives. By comparing the output maps in Figs 15–20 to the input maps in Figs 9–14 one gets an impression of the distortions introduced by the smoothed (and therefore slightly erroneous) velocity model. For more dedicated studies concerning sensitivity of mapped reflectors with respect to the velocity model, see e.g., Parkes and Hatton (1987).

CONCLUSIONS

Considering non-converted primary-reflected waves, the geological dip and curvature of a reflector can be expressed in terms of the traveltime and its first and second derivatives in the time-migration domain. The obtained expressions extend previous results in the literature to fully anisotropic and heterogeneous layered media. In addition, the formulation uses the machinery of surface-to-surface paraxial matrices, making the derivations more simple and transparent. Potential application of the obtained results can be, for example, the construction of selected reflectors in depth to help setting constraints for velocity-model building. The presented image-ray

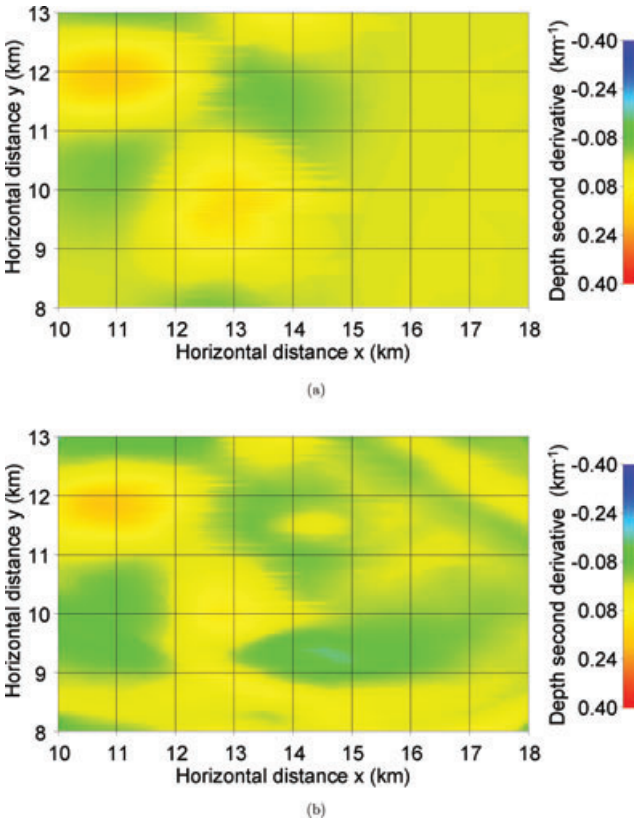

Figure 19 Second derivative *yy* a) of the true depth reflector and b) estimated by the image-ray migration method.

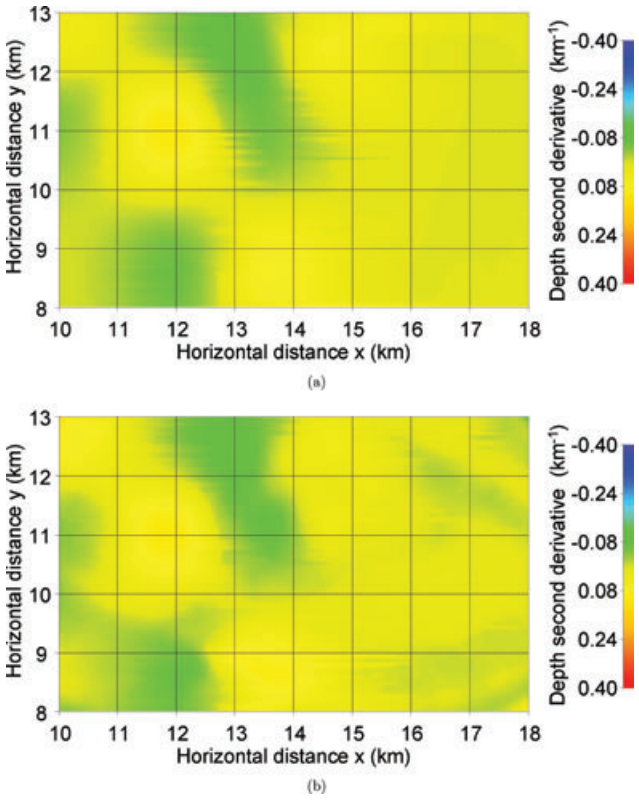

Figure 20 Second derivative *xy* a) of the true depth reflector and b) estimated by the image-ray migration method.

migration technique relies on consistency with respect to the time-migration process applied previously to the seismic data. One can therefore foresee its results used for the purpose of verifying and improving time-migration algorithms. In this way, the image-ray migration results can be seen as complementary to those obtained by normal-ray (map) migration of reflection-time parameters in the recording domain. For both mapping approaches, smoothing of the velocity field and the measured input parameters is of ultimate importance, especially concerning estimation of reflector curvature. Synthetic examples confirm the theoretical results and are encouraging for further testing and realistic applications.

ACKNOWLEDGEMENTS

We acknowledge support of the present work by VISTA, the Research Council of Norway via the ROSE project and NORSAR's SIP project 194064/I30, the National Council of Scientific and Technological Development (CNPq), Brazil, the sponsors of the Wave Inversion Technology (WIT) Consortium, Germany and the members of the Geo-Mathematical Imaging Group, USA.

REFERENCES

Bilette F. and Lambaré G. 1998. Velocity macro-model estimation from seismic reflsection data by stereotomography. *Geophysical Journal International* **135**, 671–690.

Biloti R., Santos L.T. and Tygel M. 2002. Multiparametric traveltime inversion. *Studia Geophysica et Geodaetica* **46**, 177–192.

Bortfeld R., 1989. Geometrical ray theory: Rays and traveltimes in seismic systems (second-order approximation of the traveltimes). *Geophysics* **54**, 342–349.

Cameron M.K., Fomel S. and Sethian J.A. 2006. Seismic velocity estimation and time to depth conversion of time-migrated images. 76th SEG meeting, New Orleans, Louisiana, USA, Expanded Abstracts, 3066–3070.

Cameron M.K., Fomel S. and Sethian J.A. 2007. Seismic velocity estimation from time migration. *Inverse Problems* **23** 1329–1369.

Cameron M.K. Fomel S. and Sethian J.A. 2008. Time-to-depth conversion and seismic velocity estimation using time-migration velocity. *Geophysics* **73**, VE205–VE210.

Červený V. 2001. *Seismic Ray Theory*. Cambridge University Press.
Claerbout J.F. 1992. *Earth Soundings Analysis: Processing Versus Inversion*. Blackwell Scientific Publications.
Douma H. and de Hoop M.V. 2006. Explicit expressions for prestack map time migration in isotropic and VTI media and the applicability of map depth migration in heterogeneous anisotropic media. *Geophysics* **71**, S13–S28.
Duveneck E. 2004. Velocity model estimation with data-derived wavefront attributes. *Geophysics* **69**, 265–274.
Fomel S. 2002. Application of plane-wave destruction filters. *Geophysics* **67**, 1946–1960.
Fomel S. 2007. Velocity-independent time-domain seismic imaging using local event slopes. *Geophysics* **72**, S139–S147.
Gjøystdal H. and Ursin B. 1981. Inversion of reflection times in three-dimensions. *Geophysics* **46**, 972–983.
Hertweck T. Jäger C. Mann J. Duveneck E. and Heilmann Z. 2004. A seismic reflection imaging workflow based on the common-relection-surface (CRS) stack: Theoretical background and case study. 74th SEG meeting, Denver, Colorado, USA, Expanded Abstracts, 2032–2035.
Hubral P. 1977. Time migration - Some ray theoretical aspects. *Geophysical Prospecting* **25**, 738–745.
Hubral P. and Krey T. 1980. *Interval Velocities from Seismic Reflection Time Measurements*. SEG.
Iversen E. 2005. Tangent vectors of isochron rays and velocity rays expressed in global Cartesian coordinates. *Studia Geophysica et Geodaetica* **49**, 525–540.
Iversen E. Åstebøl K. and Gjøystdal H. 1987. Time-to-depth conversion of 3D seismic interpretation data by use of 'dynamic image rays'. 49th EAEG meeting, Belgrade, Yugoslavia (now Serbia), Expanded Abstracts, 16.
Iversen E. Åstebøl K. and Gjøystdal H. 1988. 3D time-to-depth conversion of interpreted time-migrated horizons by use of the paraxial image ray method. Research report NORSAR, Norway.
Iversen E. and Gjøystdal H. 1984. Three-dimensional velocity inversion by use of kinematic and dynamic ray tracing. 54th SEG meeting, Atlanta, Georgia, USA, Expanded Abstracts, 643–645.
Iversen E. and Tygel M. 2008. Image-ray tracing for joint 3D seismic velocity estimation and time-to-depth conversion. *Geophysics* **73**, P99–P114.
Kleyn A.H. 1977. On the migration of reflection time contour maps. *Geophysical Prospecting* **25**, 125–140.
Landa E. Gurevich B. Keydar S. and Trachtman P. 1999. Application of multifocus for subsuface imaging. *Applied Geophysics* **42**, 263–300.
Moser T.J. and Červený V. 2007. Paraxial ray methods for anisotropic inhomogeneous media. *Geophysical Prospecting* **55**, 21–37.
Parkes G. and Hatton L. 1987. Towards a systematic understanding of the effects of velocity model errors on depth and time migration of seismic data. *First Break* **5**, 121–133.
Robein E. 2003. *Velocities, Time-imaging and Depth-imaging in Reflection Seismics. Principles and Methods*. EAGE.
Samson P. and Mallet J.L. 1997. Curvature analysis of triangulated surfaces in structural geology. *Mathematical Geology* **29**, 391–412.
Schleicher J. Tygel M. and Hubral P. 2007. *Seismic True-amplitude Imaging*. SEG.
Ursin B. 1982. Time-to-depth migration using wavefront curvature. *Geophysical Prospecting* **30**, 261–280.
Yilmaz O. 2000. *Seismic Data Analysis, Vol. 1*. SEG.

APPENDIX A: SURFACE-TO-SURFACE TRAVELTIME RELATIONS FOR THE IMAGE-RAY FIELD

In this appendix we derive transformations pertaining to an exploding-surface ray field, i.e., a ray field where individual rays are started simultaneously at a given initial (so-called anterior) surface. The slowness vectors of the rays are normal to this surface. The rays are captured on a final (so-called posterior) surface. The image-ray field is a special case of such exploding-surface ray fields. The initial surface is then the datum surface, while the final surface is the reflector.

We denote the standard ray coordinates for the image-ray field as $\hat{\boldsymbol{\gamma}} = (m_1, m_2, t)^T$. Here, t is the traveltime from the exploding initial surface, $\mathcal{M}$. On the surface $\mathcal{M}$ itself we therefore have $t = 0$. As indicated in the main text, we let the datum surface be planar horizontal. Points on that plane are located by Cartesian coordinates, $\mathbf{m}$. Such considerations do not imply essential loss of generality, as the extension to permit a curved datum surface is straightforward. A fixed, reference (central) image ray is specified by its starting point at $O^{\mathcal{M}}$, where $\mathbf{m} = \mathbf{0}$ (Fig. A1). The ray hits the reflector surface $\mathcal{Z}$ at the point $O^{\mathcal{Z}}$. Moreover, in the following we take advantage of an alternative ray coordinate system for the exploding-surface ray field, described by the vector $\hat{\boldsymbol{\mu}} = (m_1, m_2, t^{\mathcal{Z}})^T$. Here the parameter $t^{\mathcal{Z}}$ is the traveltime measured from the surface $\mathcal{Z}$, along which we have $t^{\mathcal{Z}} = 0$.

The traveltime parameters t and $t^{\mathcal{Z}}$ are independent variables. However, for a point on a given ray, specified by the vector $\mathbf{m}$, we can connect the two parameters via the relation

$$t^{\mathcal{Z}} = t - \mathcal{T}, \tag{A1}$$

where $\mathcal{T}$ denotes the surface-to-surface traveltime. We remark that the definition (A1) was chosen so that both traveltimes, t and $t^{\mathcal{Z}}$, increase along propagation of the reference image ray. For an illustration of the traveltime concepts in equation (A1), see Fig. A1.

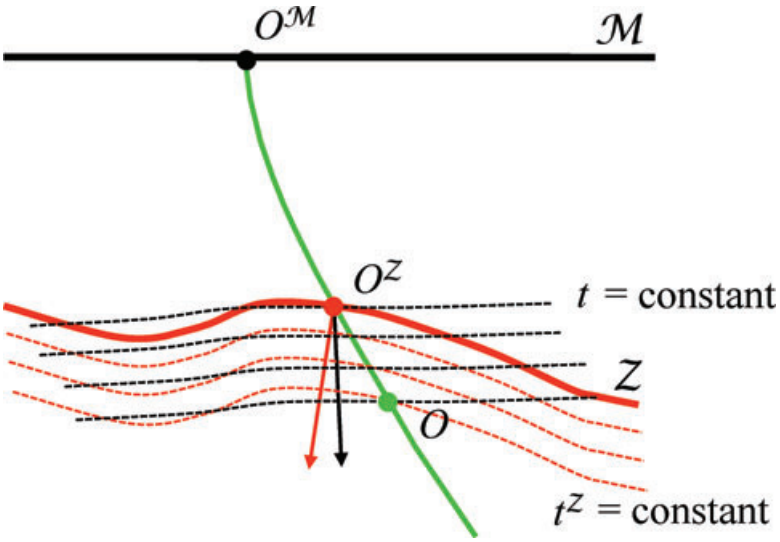

Figure A1 Traveltime concepts associated with the image-ray trajectory (green): $\mathcal{T}$ is the (surface-to-surface) time between the point $O^{\mathcal{M}}$ in the datum surface $\mathcal{M}$ (solid black) and the point $O^{\mathcal{Z}}$ in the reflector surface $\mathcal{Z}$ (solid red); t is the time from $O^{\mathcal{M}}$ to a general point O on the image ray; $t^{\mathcal{Z}}$ is the time from $O^{\mathcal{Z}}$ to O. Some contours $t =$ constant (dashed black) and $t^{\mathcal{Z}} =$ constant (dashed red) are indicated in the vicinity of the point $O^{\mathcal{Z}}$. The gradient directions corresponding to the traveltimes t and $t^{\mathcal{Z}}$ at $O^{\mathcal{Z}}$ are signified, respectively, by black and red arrows.

General properties

Let S be an arbitrary differentiable variable which can be either a function of the ray coordinates $\hat{\boldsymbol{\mu}}$ or the local Cartesian reflector coordinates $\hat{\mathbf{z}}$. The chain rule for derivatives then yields

$$\frac{\partial S}{\partial \mu_i} = \frac{\partial S}{\partial z_m}\frac{\partial z_m}{\partial \mu_i}. \tag{A2}$$

In particular, if $S = \mu_k$, one obtains the well-known relation between the forward transformation matrix $(\partial z_m/\partial \mu_i)$ and its inverse $(\partial \mu_k/\partial z_m)$,

$$\frac{\partial \mu_k}{\partial z_m}\frac{\partial z_m}{\partial \mu_i} = \delta_{ki}. \tag{A3}$$

We make the following observations:

- The partial derivatives $\partial z_M/\partial m_I$ are taken for constant $t^{\mathcal{Z}}$. When $t^{\mathcal{Z}} = 0$ we can identify these derivatives as the elements of 2×2 submatrix $\boldsymbol{\mathcal{A}}$ of the 4×4 surface-to-surface paraxial matrix, i.e.,

$$\mathcal{A}_{MI} = \frac{\partial z_M}{\partial m_I}. \tag{A4}$$

- The first partial derivatives of z_3 with respect to m_I are also taken for constant $t^{\mathcal{Z}}$. When $\mathbf{m} = \mathbf{0}$ and $t^{\mathcal{Z}} = 0$, we have

$$\frac{\partial z_3}{\partial m_I} = 0. \tag{A5}$$

  To derive the above result, we observe that, if $t^{\mathcal{Z}} = 0$, points are on the reflector, namely $z_3 = \Sigma(\mathbf{z})$. As a consequence, keeping $t^{\mathcal{Z}} = 0$, we have

$$\frac{\partial z_3}{\partial m_I} = \frac{\partial \Sigma}{\partial z_M}\frac{\partial z_M}{\partial m_I}. \tag{A6}$$

  equation (A5) now follows, since $\mathbf{z} = \mathbf{0}$ when $\mathbf{m} = \mathbf{0}$, $t^{\mathcal{Z}} = 0$, and also $(\partial \Sigma/\partial z_M)(\mathbf{0}) = 0$.

- Partial differentiation with respect to t and $t^{\mathcal{Z}}$ is equivalent, since $\mathbf{m}$ is kept constant in both situations. Therefore, we have

$$\frac{\partial z_M}{\partial t^{\mathcal{Z}}} = \frac{\partial z_M}{\partial t} = v_M^{\mathcal{Z}}, \qquad \frac{\partial z_3}{\partial t^{\mathcal{Z}}} = \frac{\partial z_3}{\partial t} = v_3^{\mathcal{Z}}. \tag{A7}$$

- Considering only differentiation with respect to the first two components $\mu_I = m_I$ of $\hat{\boldsymbol{\mu}}$ in equation (A2) one can write

$$\frac{\partial S}{\partial m_I} = \frac{\partial S}{\partial z_M}\frac{\partial z_M}{\partial m_I} + \frac{\partial S}{\partial z_3}\frac{\partial z_3}{\partial m_I}. \tag{A8}$$

  Differentiation with respect to $\mathbf{m}$ in equation (A8) is, by definition, performed for constant $t^{\mathcal{Z}}$. If $\mathbf{m} = \mathbf{0}$ and $t^{\mathcal{Z}} = 0$ we use equation (A5) to obtain

$$\frac{\partial S}{\partial m_I} = \frac{\partial S}{\partial z_M}\frac{\partial z_M}{\partial m_I}. \tag{A9}$$

- The situation $k = 3$ in equation (A3) is described specifically by the equations

$$\frac{\partial t^{\mathcal{Z}}}{\partial z_M}\frac{\partial z_M}{\partial m_I} + \frac{\partial t^{\mathcal{Z}}}{\partial z_3}\frac{\partial z_3}{\partial m_I} = 0, \qquad \frac{\partial t^{\mathcal{Z}}}{\partial z_M}\frac{\partial z_M}{\partial t^{\mathcal{Z}}} + \frac{\partial t^{\mathcal{Z}}}{\partial z_3}\frac{\partial z_3}{\partial t^{\mathcal{Z}}} = 1. \tag{A10}$$

  Using equations (A5) and (A7) for $\mathbf{m} = \mathbf{0}$ and $t^{\mathcal{Z}} = 0$ then gives

$$\frac{\partial t^{\mathcal{Z}}}{\partial z_I} = 0, \qquad \frac{\partial t^{\mathcal{Z}}}{\partial z_3} = \frac{1}{v_3^{\mathcal{Z}}}. \tag{A11}$$

Surface-to-surface traveltime relation: first order

Differentiating equation (A1) with respect to $\mathbf{z}$ yields

$$\frac{\partial t^{\mathcal{Z}}}{\partial z_M} = \frac{\partial t}{\partial z_M} - \frac{\partial \mathcal{T}}{\partial z_M}, \qquad \frac{\partial t^{\mathcal{Z}}}{\partial \mathbf{z}} = \frac{\partial t}{\partial \mathbf{z}} - \frac{\partial \mathcal{T}}{\partial \mathbf{z}}. \tag{A12}$$

Using $S = \mathcal{T}$ in equation (A9),

$$\frac{\partial \mathcal{T}}{\partial m_I} = \frac{\partial z_M}{\partial m_I}\frac{\partial \mathcal{T}}{\partial z_M}, \qquad \frac{\partial \mathcal{T}}{\partial \mathbf{m}} = \boldsymbol{\mathcal{A}}^T \frac{\partial \mathcal{T}}{\partial \mathbf{z}}, \tag{A13}$$

and the fact that $\partial t^{\mathcal{Z}}/\partial \mathbf{z} = \mathbf{0}$ then shows that the vector form of equation (A12) can be restated as

$$\frac{\partial t}{\partial \mathbf{z}} = \boldsymbol{\mathcal{A}}^{-T}\frac{\partial \mathcal{T}}{\partial \mathbf{m}}. \tag{A14}$$

Equation (A14) is a fundamental equation that can be used to relate the dip of the reflector to the gradient, $\partial\mathcal{T}/\partial\mathbf{m}$, of surface-to-surface traveltime. The vector $\partial t/\partial \mathbf{z}$ contains the first two components of the slowness vector at the point $O^{\mathcal{Z}}$. This slowness vector projection belongs to the local Cartesian ($\mathbf{z}$, z_3) coordinate system and is equivalently referred to as

$$\mathbf{p}^{\mathcal{Z}} = \frac{\partial t}{\partial \mathbf{z}}. \tag{A15}$$

Surface-to-surface traveltime relation: second order

We differentiate the leftmost equation (A10) with respect to components m_J as follows,

$$\frac{\partial}{\partial m_J}\left(\frac{\partial t^{\mathcal{Z}}}{\partial z_M}\frac{\partial z_M}{\partial m_I} + \frac{\partial t^{\mathcal{Z}}}{\partial z_3}\frac{\partial z_3}{\partial m_I}\right) = 0. \tag{A16}$$

Working out the various terms yields

$$\frac{\partial z_M}{\partial m_I}\frac{\partial}{\partial m_J}\left(\frac{\partial t^{\mathcal{Z}}}{\partial z_M}\right) + \frac{\partial t^{\mathcal{Z}}}{\partial z_3}\frac{\partial^2 z_3}{\partial m_I \partial m_J} + \ldots = 0, \tag{A17}$$

where the dots (...) signify terms that contain partial derivatives of the type $\partial z_3/\partial m_I$ or $\partial t^{\mathcal{Z}}/\partial z_M$. For $\mathbf{m} = \mathbf{0}$ and $t^{\mathcal{Z}} = 0$ all such terms are zero. We now apply equation (A1) in equation (A17) and insert the surface function $z_3 = \Sigma^{\mathcal{Z}}(\mathbf{z})$. Elaborating equation (A17) further utilizing the general differential operator in equation (A8), and finally requiring $\mathbf{m} = \mathbf{0}$ and $t^{\mathcal{Z}} = 0$, we obtain

$$\frac{\partial^2 \mathcal{T}}{\partial m_I \partial m_J} = \frac{\partial z_M}{\partial m_I}\left(\frac{\partial^2 t}{\partial z_M \partial z_N} + \frac{\partial t^{\mathcal{Z}}}{\partial z_3}\frac{\partial^2 \Sigma^{\mathcal{Z}}}{\partial z_M \partial z_N}\right)\frac{\partial z_N}{\partial m_J}. \tag{A18}$$

In the above derivations, we have made use of the results

$$\frac{\partial z_M}{\partial m_I}\frac{\partial}{\partial m_J}\left(\frac{\partial t}{\partial z_M}\right) = \frac{\partial z_M}{\partial m_I}\frac{\partial^2 t}{\partial z_M \partial z_N}\frac{\partial z_N}{\partial m_J}, \tag{A19}$$

and

$$\frac{\partial z_M}{\partial m_I}\frac{\partial}{\partial m_J}\left(\frac{\partial \mathcal{T}}{\partial z_M}\right) = \frac{\partial z_M}{\partial m_I}\frac{\partial}{\partial z_M}\left(\frac{\partial \mathcal{T}}{\partial m_J}\right) = \frac{\partial^2 \mathcal{T}}{\partial m_I \partial m_J}, \tag{A20}$$

as well as the properties (4) of the reflector. Using the rightmost equation (A11) and also the definition of the reflector curvature matrix

$$D_{MN} = -\frac{\partial^2 \Sigma^{\mathcal{Z}}}{\partial z_M \partial z_N}, \tag{A21}$$

also given by equation (4), our final result in component form appears as

$$\frac{\partial^2 \mathcal{T}}{\partial m_I \partial m_J} = \frac{\partial z_M}{\partial m_I}\left(\frac{\partial^2 t}{\partial z_M \partial z_N} - \frac{1}{v_3^Z} D_{MN}\right)\frac{\partial z_N}{\partial m_J}. \tag{A22}$$

The corresponding matrix form of equation (A22) is

$$\frac{\partial^2 \mathcal{T}}{\partial \mathbf{m}^2} = \boldsymbol{\mathcal{A}}^T\left(\frac{\partial^2 t}{\partial \mathbf{z}^2} - \frac{1}{v_3^Z}\mathbf{D}\right)\boldsymbol{\mathcal{A}}. \tag{A23}$$

equation (A23) is a fundamental relation that relates the curvature matrix, $\mathbf{D}$, of the reflector to the second derivatives of the surface-to-surface traveltime, $\partial^2\mathcal{T}/\partial\mathbf{m}^2$.

The matrix $\partial^2 t/\partial \mathbf{z}^2$ contains second derivatives of the traveltime from the datum surface taken along the tangent plane of the reflector. We can therefore compute this matrix as

$$\frac{\partial^2 t}{\partial \mathbf{z}^2} = \mathbf{E} + \boldsymbol{\mathcal{A}}^{-T}\mathbf{Q}_1^T\mathbf{P}_1. \tag{A24}$$

The above matrix is a special version of the product $\boldsymbol{\mathcal{C}}\boldsymbol{\mathcal{A}}^{-1}$, in which $\boldsymbol{\mathcal{C}}$ is evaluated with zero reflector curvatures.

APPENDIX B: RAY-VELOCITY VECTOR COMPONENT NORMAL TO THE REFLECTOR

In this appendix the component v_3^Z of the ray-velocity vector is expressed in terms of the scalar κ defined in equation (30). We start from the relation

$$z_3 = \boldsymbol{\nu}^{Y^T}\mathbf{y} + n_3^Z y_3 = n_3^Z\left(y_3^Z - \mathbf{f}^T\mathbf{y}\right), \tag{B1}$$

obtained from the relationship between $\hat{\mathbf{y}}$- and $\hat{\mathbf{z}}$-coordinates, as described by equations (7) and (10), and also taking into account equation (12). Differentiation of both sides with respect to t, yields

$$v_3^Z = n_3^Z\left(v_3^Y - \mathbf{f}^T\mathbf{v}^Y\right), \tag{B2}$$

where we recalled that $v_3^Z = dz_3/dt$, $v_3^Y = dy_3/dt$ and $\mathbf{v}_3^Y = d\mathbf{y}/dt$. Substitution of $\mathbf{f}$ given by equation (29) and after some rearrangement recovers relation (33).